3. EQUILIBRIUM, STABILITY, AND TRANSPORT

Y-K. Martin Peng
John T. Hogan
Marc L. Klaski
Dennis J. Strickler
Charles G. Bathke
Erfan Ibrahim
James A. Leuer
David J. Ward
David A. Ehst
Stephen C. Jardin
Tak-Kuen Mau
John C. Whitson

Contents

3. EQUILIBRIUM, STABILITY, AND TRANSPORT

3.1. INTRODUCTION

The ARIES-I design is a conceptual commercial reactor based on modest extrapolation from the present tokamak physics data base. For a commercial reactor, steady-state operation is preferable because of the many undesirable features of pulsed operation (such as thermal fatigue of in-vessel components and magnets and the requirement for a thermal-energy storage system), which lead to a short reactor lifetime and high costs. For an economical steady-state reactor, the recirculating power fraction should be <20%. This can be achieved by reducing the amount of plasma current to be driven by external means (*i.e.*, minimizing the total plasma current and maximizing the bootstrap-current fraction) and also by using an efficient, cost-effective current-drive technique.

The ARIES-I design operates at a relatively high plasma aspect ratio ($A = 4.5$), a low plasma current ($I_p = 10.2$ MA), and a high on-axis magnetic field ($B_o = 11.3$ T). As a result, the poloidal beta is high and a high bootstrap-current fraction of 0.68 is predicted. Because of the low plasma current and high bootstrap-current fraction, only 3.3 MA of current should be driven by external means. Therefore, a steady-state reactor with relatively small current-drive power is possible. Systems-code analysis confirms that an optimum first-stability tokamak reactor operates with high aspect ratio, low current, and high bootstrap-current fraction. The key parameters of the ARIES-I reactor are listed in Table 3.1-I.

The ARIES-I reactor parameters are found through extensive and self-consistent iterations among magnetohydrodynamic (MHD) equilibrium and stability, transport, current-drive, and edge-physics analyses. Engineering constraints imposed by system integration for a power reactor have also been taken into account. In the areas of MHD equilibrium and stability and plasma transport, the regime of operation of the ARIES-I plasma is different from current tokamak experiments in many aspects including:

1. Operating at a relatively high plasma aspect ratio ($A \equiv 1/\epsilon = 4.5$), a low plasma current ($I_p = 10.2$ MA), a high poloidal beta ($\epsilon\beta_p = 0.7$), and plasma current profiles characterized by on-axis safety factor, $q_o \approx 1.3$, and 95% flux safety factor, $q_{95} > 4$.

Table 3.1-I.
Key Parameters of the ARIES-I Reactor

Major radius, R (m)	6.75
Minor plasma radius, a (m)	1.50
Aspect ratio, A	4.50
Elongation, κ_x	1.80
Triangularity, δ_x	0.70
Magnetic field at coil, B_c (T)	21.00
Magnetic field on axis, B_o (T)	11.33
Plasma current, I_p (MA)	10.20
Safety factor on axis, q_o	1.30
Edge safety factor, q^*	3.90
Peak electron density, n_{e0} (10^{20} m^{-3})	1.88
Average electron density, n_e (10^{20} m^{-3})	1.45
Separatrix electron density, n_s (10^{20} m^{-3})	0.87
Peak electron temperature, T_{e0} (keV)	36.62
Average (density-weighted) electron temperature, T_e (keV)	19.30
Volume-averaged electron temperature, $\bar{T}_e$ (keV)	17.44
Toroidal beta, β_t (%)	1.90
Effective charge, Z_{eff}	1.65
Bootstrap-current fraction, I_{BS}/I_p	0.68

2. Operating at $A \equiv 1/\epsilon = 4.5$ and placing the poloidal-field (PF) coils outside the toroidal-field coils leads to large stored energy in the PF coils. Minimizing this energy will place constraints on the choice of plasma elongation, κ, and triangularity, δ. The MHD equilibrium analysis is reported in Sec. 3.2.

3. Operating at MHD-stability beta limit against high-n ballooning and $n = 1$ kink modes with the conductive wall at infinity and using plasma profiles consistent with current-drive (driven current density) and transport (flat density and narrow temperature profiles) analyses. The MHD β limit is discussed in Sec. 3.3.

4. Placing the passive conductor for stabilizing the vertical motion of the plasma behind the blanket, which reduces the engineering constraints (cooling, neutron damage, *etc.*), leads to a reduced plasma elongation, $\kappa_x = 1.8$. The vertical stability of the ARIES-I plasma is considered in Sec. 3.4.

5. Operating an ignited plasma with high synchrotron radiation caused by high on-axis magnetic field, high electron temperature, and a poorly reflective first wall. Absence of deep fueling techniques leads to a flat density profile. The time-dependent transport analysis of the ARIES-I plasma is presented in Sec. 3.5.

3.2. MHD EQUILIBRIUM

3.2.1. Minimizing Stored Energy of Poloidal-Field Coils

Operating at $A \equiv 1/\epsilon = 4.5$ and placing the poloidal-field (PF) coils outside the toroidal-field (TF) coils leads to large stored energy in the PF coils. In this section, a prescription for choosing plasma shape (plasma elongation, κ, and triangularity, δ) to minimize this stored energy is presented.

Placing the ARIES-I PF coils external to the TF coils permits the use of a multipole expansion technique [1, 2] to describe accurately the PF-coil magnetic fields used in MHD equilibrium computations performed with the tokamak simulation code (TSC) [3] or the HEQ code [4]. Limiting the multipole expansion to hexapole and lower moments minimizes the number of dependent variables required to describe the plasma shape. Using the multipole expansion technique to examine plasma equilibria parametrically for a range of plasma elongation and triangularity values resulted in a prescription for minimizing the PF-coil stored energy, W_{PF}, which is used in the ARIES systems code (Sec. 2).

The TSC was modified so that the poloidal flux produced by a PF-coil set could be determined by specifying either the PF-coil locations and currents or the amplitudes of the even and odd nullapole, dipole, quadrupole, hexapole, and octopole moments, and the even decapole moment in the multipole expansion series [1]. In addition, the TSC was modified to perform the inverse operation of decomposing the poloidal flux produced by a PF-coil set into the multipole components of the same truncated series. The TSC was then used to analyze parametrically the equilibrium of the interim design point I given in Table 3.2-I.

Since the PF coils are relatively far from the plasma, the cost of the coils to produce the higher order multipoles is high, making them undesirable. Therefore, in this analysis, the multipole expansion was limited to hexapole and lower moments, thereby reducing the number of variables. The plasma current, toroidal field, profile form factors (Sec. 3.2.2), major and minor radii, and the nullapole and dipole moments were held

Table 3.2-I.
Fixed Parameters for TSC Parametric Equilibrium Analysis

Interim design point	I	II
Plasma current, I_p (MA)	7.26	10.5
Toroidal field, B_t (T)	12.38	12.72
Profile form factors		
α	−3.0	−3.0
γ	−2.5	−3.0
β_J	3.24	1.94
Major radius, R_o (m)	6.0	6.12
Minor radius, a (m)	1.0[a]	1.36
Nullapole current equivalent (MA)	0.351	0.271
Dipole current equivalent (MA)	0.429	0.517

[a]For $A = 4.5$, $a = 1.333$.

fixed at the interim design values. The ratio of the hexapole to quadrupole amplitudes was selected as the dependent variable. The absolute magnitudes of these two amplitudes were determined as the minimum amplitudes that are necessary to produce a separatrix with the specified minor radius. This algorithm, subsequently, generates a set of plasma equilibria that requires only low-order multipoles which can be efficiently produced by the external PF coils. Consequently, the external field solutions have minimum PF-coil current, $\sum |I_{PF}|$, and, hence, minimum W_{PF}. Because both plasma triangularity, δ, and elongation, κ, vary as the ratio of the quadrupole to hexapole moment varies, this algorithm yields the δ that minimizes the PF-coil stored energy, W_{PF}, for a given κ.

The results of this analysis are shown in Fig. 3.2-1. Plasmas with shapes corresponding to the region below the δ-κ correlation of Fig. 3.2-1(A) would not have a separatrix, and those above the correlation would either have a smaller minor radius (larger A) or would require higher multipole moments and larger W_{PF} to maintain the same minor radius. This analysis also produced the correlation between the equivalent multipolar current, which scales approximately as the square root of W_{PF}, and κ. This correlation, shown in Fig. 3.2-1(B), indicates that W_{PF} increases as κ is decreased (δ increases) for the range of $1 < \kappa < 2.7$ considered. It was found, however, that this W_{PF}-κ correlation did not have a significant impact on determining the final design values of κ and δ (Sec. 2).

To pursue further the issue of minimizing W_{PF}, a code (FLXCON) was developed to determine the locations and currents of a PF-coil set that would reproduce the flux pattern of a given set of multipole moments. The FLXCON code moves the coils along a specified surface while minimizing an object function defined as the sum of two terms. The first term measures the relative error with which the coils reproduce the flux of the given set of multipole moments on a test surface representative of the plasma surface and the second term measures W_{PF}. To illustrate the use of FLXCON, an HEQ-generated equilibrium for interim design point II (Table 3.2-I) was modeled with TSC using the same set of 12 PF coils with 6 current groups; the HEQ and TSC results are given for comparison in Table 3.2-II. The small differences in R_T, a, and κ_x between the HEQ and TSC results are directly attributable to numerical inaccuracies due to finite grid size in both codes. The multipole decomposition of the PF-coil flux was used to generate three sets of six PF coils and six current groups labeled DEC, OCT, and HEX in Table 3.2-II to denote the maximum multipole moment used. As the higher moments are eliminated, $\sum |I_{PF}|$ decreases as expected, but W_{PF} is lower only for the HEX case. The plasma shape, however, drifts from the base shape because the higher moments were used inefficiently to suppress κ and to provide additional triangularity. A more

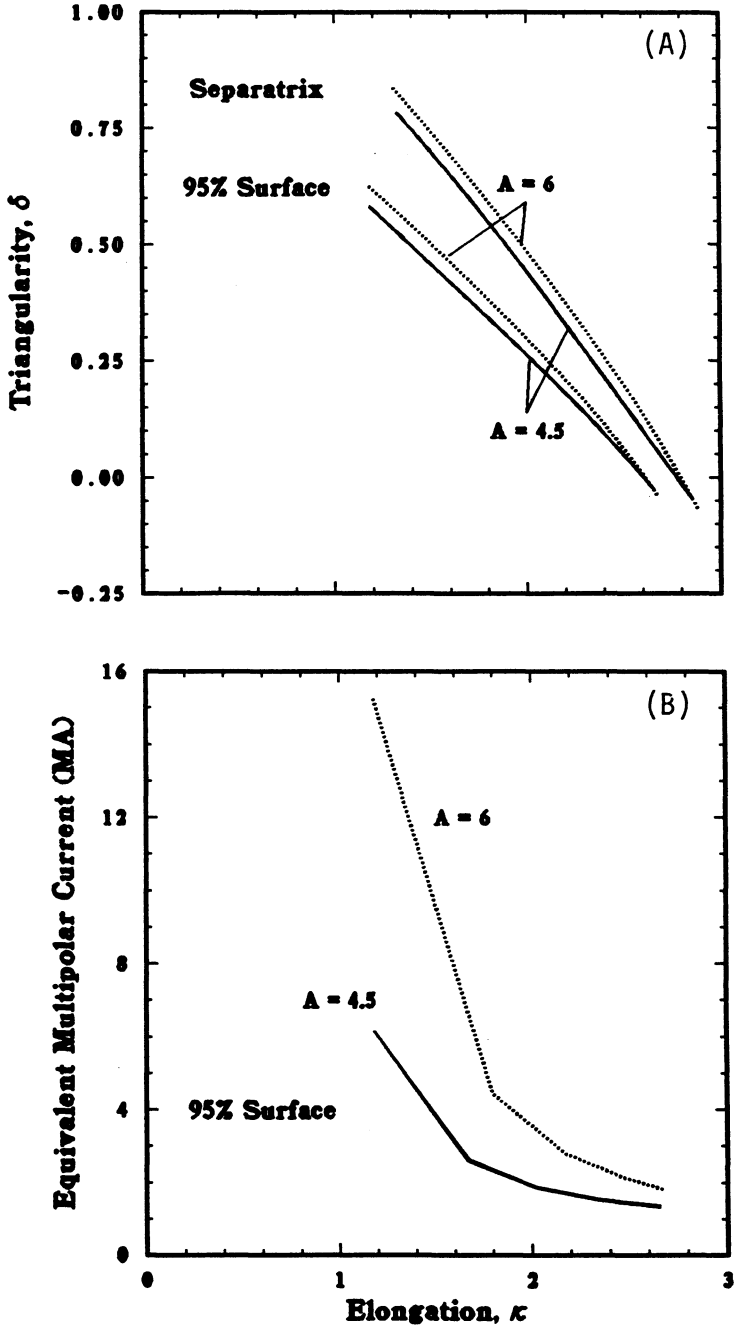

Figure 3.2-1. The correlation between (A) plasma triangularity and elongation, which minimizes the PF-coil stored energy, and (B) the equivalent multipolar current ($\propto W_{PF}^{1/2}$) and elongation of the 95% flux surface. (Analysis performed for the interim design point I of Table 3.2-I with $A = 4.5$ and $A = 6$.)

Table 3.2-II.
Equilibrium Calculations with Different Multipole Moments for Interim Design Point II of Table 3.2-I

	HEQ[a]	BASE[a]	DEC[b]	OCT[b]	HEX[b]
Major radius, R_o (m)	6.12	6.12	6.12	6.13	6.13
Minor radius, a (m)	1.36	1.35	1.35	1.34	1.34
Magnetic axis, R_M (m)	6.33	6.35	6.35	6.35	6.34
Elongation					
κ_x	1.75	1.73	1.68	1.70	1.84
κ_{95}	1.58	1.59	1.55	1.56	1.67
Triangularity					
δ_x	0.74	0.77	0.75	0.68	0.46
δ_{95}	0.48	0.50	0.49	0.47	0.36
Separatrix coordinates (m)					
R_x	5.11	5.12	5.14	5.25	5.51
z_x	2.38	2.39	2.31	2.32	2.53
Toroidal beta, β (%)	1.84	1.86	1.94	1.98	1.86
Poloidal beta, β_p	1.85	1.77	1.78	1.78	1.74
Plasma volume (m^3)	347	348	337	329	343
Safety factor					
$q_{(0)}$	1.59	1.59	1.54	1.50	1.58
$q_{(a)}$	7.84	7.02	6.46	6.19	6.52
Current, $\sum \lvert I_{PF} \rvert$ (MA)	142	142	114	111	82
Stored energy, W_{PF} (GJ)	7.57	7.57	7.78	8.10	6.80

[a]PF-coil flux determined by PF-coil currents and locations using HEQ and TSC (BASE) codes.

[b]PF-coil flux determined by truncated multipole-expansion series with up to decapole (DEC), octopole (OCT), and hexapole (HEX) moments.

efficient method to generate the same plasma shape would require less quadrupole and more hexapole moments, and will be used in the future.

3.2.2. Free-Boundary MHD Equilibria and Operational Requirements

Given the coil distribution, reference MHD equilibria for ARIES-I are computed using the HEQ code [4], which calculates free-boundary solutions for a given plasma position, shape, and linked poloidal flux while minimizing the stored energy. The plasma shape is chosen to have $\kappa_x = 1.8$ to allow for adequate vertical stabilization (Sec. 3.4) and $\delta_x = 0.7$ based on the analysis in Sec. 3.2.1 to minimize the PF-coil stored energy. The plasma pressure profile is consistent with the transport analysis of Sec. 3.4 (flat density and narrow temperature profiles), and the current profile is consistent with first-stability operation with high $\epsilon\beta_p$ and with current-drive analysis of the driven current-density profile. These constraints led to a choice of profiles that are close to the following pressure, p, and poloidal current-profile, f', functions:

$$p(x) = p_o \left(\frac{e^{-\alpha x} - e^{-\alpha}}{e^{-\alpha} - 1} \right) , \tag{3.2-1}$$

$$f f'(x) = \mu_o R_o^2 p_o \left(\frac{1}{\beta_J - 1} \right) \left(\frac{e^{-\gamma x} - e^{-\gamma}}{e^{-\gamma} - 1} \right) , \tag{3.2-2}$$

where x is the poloidal flux normalized to 1 within the plasma. Values of $\alpha = -1.35$, $\gamma = -1.35$, and $\beta_J = 2.29$ were chosen for the equilibrium analysis. The toroidal plasma current density is

$$J_t = R p' + \frac{f f'}{\mu_o R} , \tag{3.2-3}$$

where R is in the direction of the major radius.

The poloidal-flux distribution of the intermediate ARIES-I equilibrium is given in Fig. 3.2-2. Profiles of the plasma pressure, toroidal current density, and safety factor are shown in Fig. 3.2-3. Parameters of this intermediate equilibrium that are relevant to stability and current-drive analyses are given in Table 3.2-III. The reference ARIES-I equilibrium of Table 3.1-I is essentially similar to this equilibrium (scaled to $R_o = 6.75$ m).

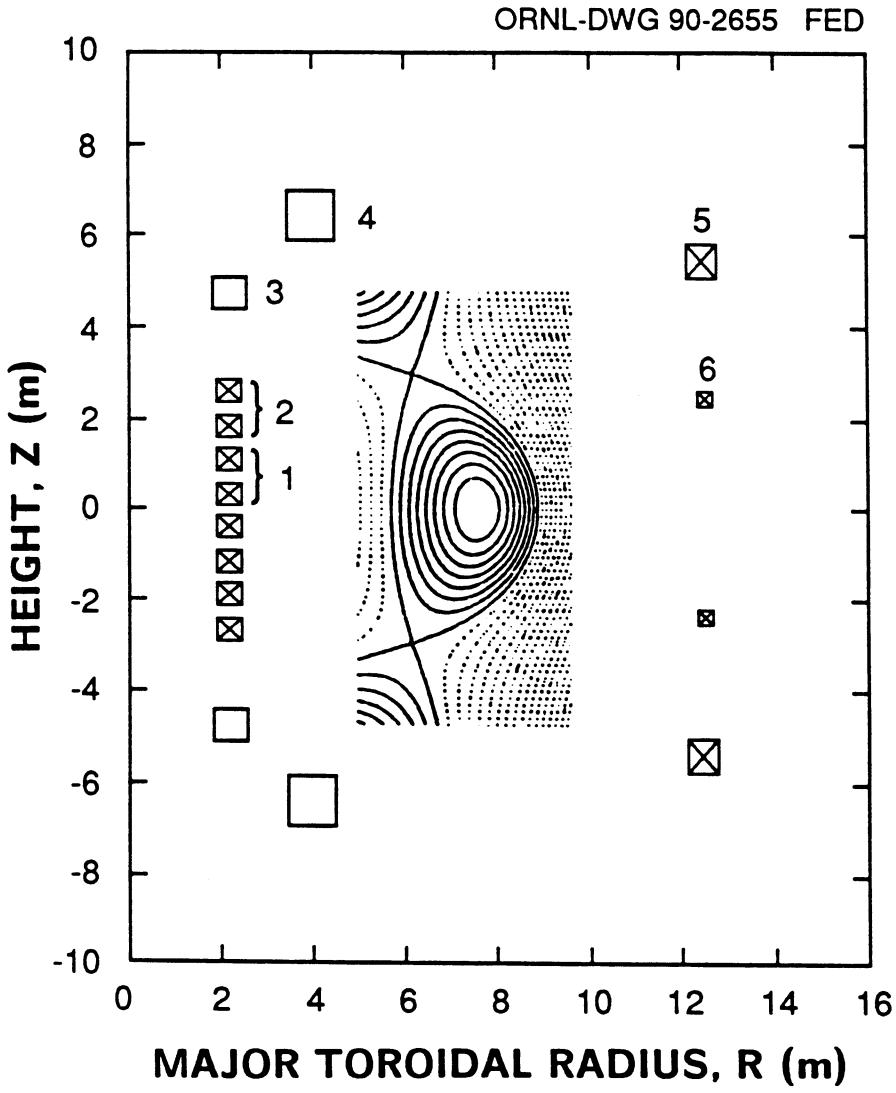

Figure 3.2-2. Plasma-equilibrium-flux configuration and PF-coil placement.

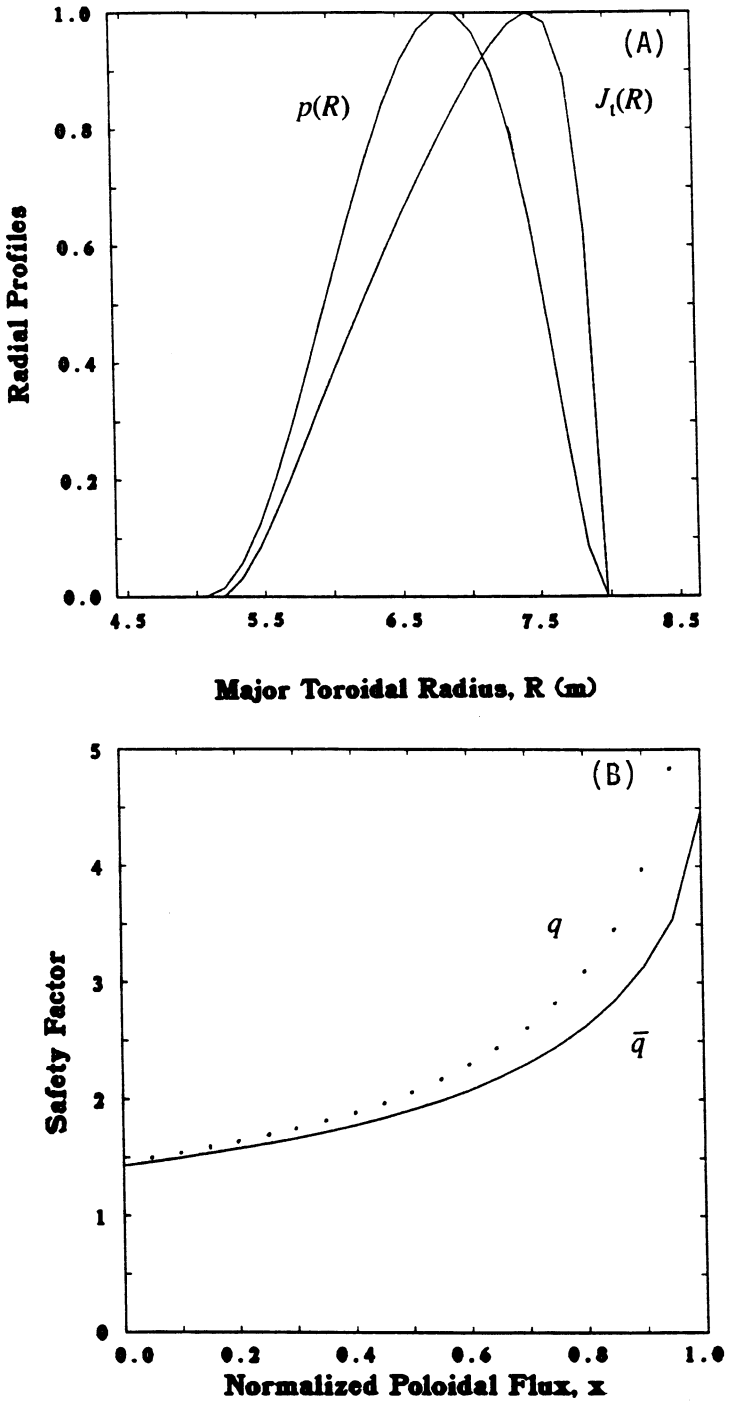

Figure 3.2-3. Profiles of (A) pressure and toroidal current density along the major radius, and (B) q and $\bar{q}$ (the average-field safety factor) along the normalized poloidal flux within the plasma edge. (For plasma equilibrium of Fig. 3.2-2.)

Table 3.2-III.
The Interim ARIES-I Divertor MHD Equilibrium[a]

Major radius, R_o (m)	7.24
Minor radius, a (m)	1.61
External toroidal field at R_o, B_t (T)	11.9
Plasma current, I_p (MA)	11.3
Safety factor on axis, q_o	1.24
Average-field safety factor, $\bar{q}$	4.45
Safety factor at 95% flux, q_{95}	4.64
Toroidal beta, β (%)	1.90
Poloidal beta, β_p	2.19
Elongation at $\times$-point, κ_x	1.80
Elongation at 95% flux, κ_{95}	1.60
Triangularity at $\times$-point, δ_x	0.70
Triangularity at 95% flux, δ_{95}	0.50
$\times$-point location	
R_x (m)	6.11
Z_x (m)	2.90
Internal inductance, l_i	0.82
Stored PF-coil energy, W_{PF} (GJ) [b]	12.0

[a] The reference equilibrium of Table 3.1-I is essentially similar this equilibrium (scaled to $R_o = 6.75$ m).

[b] Stored energy is higher at full I_p and low β.

Analysis leading to the interim MHD equilibria provided an adjustment to the conditions that relate I_p to q, a, B_t, and the plasma shape parameters. This adjusted relationship, used in systems studies, is

$$I_p \bar{q} = 5 a B_t \left[\frac{\epsilon(1.15 - 0.65\epsilon)}{(1-\epsilon^2)^2}\right]\left(\frac{1+\kappa_x^2}{2}\right), \tag{3.2-4}$$

where $\bar{q}$ is the average-field safety factor using the averaged poloidal field at the plasma edge. For this class of equilibria, the edge and 95% flux surface quantities are related through

$$\frac{\delta_x}{\delta_{95}} = 1.59\,\frac{\kappa_x}{\kappa_{95}} = (1.13 - 0.08\epsilon)\,\frac{q_{95}}{\bar{q}} = 1.09\,. \tag{3.2-5}$$

Different forms of the profile functions can be used to produce equilibria nearly identical to this case in all its global parameters, as are given in Table 3.2-III. The results of the free boundary equilibrium and the PF-coil currents do not change significantly when these different profile functions are used, as long as the global parameters remain unchanged.

Since the ARIES-I reactor uses noninductive methods to assist start-up of the plasma current (Sec. 12), the amount of poloidal flux linkage between the plasma and the PF coils can be chosen to reduce the PF-coil stored energy. Some flexibility exists near the condition of minimum stored energy to vary the PF-coil current with a fixed $\times$-point location: low beta and low linked flux, high beta and low linked flux, and high beta and high linked flux. The maximum current for each coil is then estimated and used in sizing its cross sections and locating the coil, as plotted in Fig. 3.2-2 (assuming an overall current density of 20 MA/m^2 for each coil). This data is then used as input to the engineering design of the PF-coil system (Sec. 7).

3.3. MHD-STABILITY BETA LIMIT

3.3.1. Dependences of the Beta Limit

The first stability regime requires that all ideal MHD modes be at least marginally stable in the absence of a conducting shell beyond the plasma edge [5]. While this requirement is broad in scope, it is usually adequate to examine only the high-n ballooning modes and the low-n ($n = 1$) kink modes to determine the stability beta limit. The

intermediate-n ballooning modes (the "infernal" modes) are easily avoided by retaining small gradients in the q profile near the plasma axis.

As an input to design trade-offs involving plasma shaping (profiles, A, and the β limit), our study places an emphasis on clarifying the dependences of β on A, κ_{95}, q_o, and q_{95}. We use only the traditionally successful profile functions for the analysis. This study, therefore, is limited in its scope, since several other parameters (*e.g.*, δ and the q and pressure profiles) also affect the plasma beta limit. However, this study benefits from an extensive review of the beta limit investigation recently carried out for ITER [6] and from reviews of the large body of information in the literature. Calculations are carried out for high-A (4.5 and 6.0) ARIES-I plasmas using the PEST equilibrium and stability codes [7] to "fill in" data where needed. The combined data base of the stability analysis covers a range $A = 2.6$ to 6.0, $\kappa_{95} = 1.6$ to 3.2, $q_o = 1.0$ to 2.0, and $q_{95} \leq 5$.

The pressure and safety-factor profile functions used include those optimized for the JET plasma [5] and those used in the ITER studies [6] and are given by:

$$p = p_o \left[(1 - y^{\alpha})^{\gamma} + p_1 \, y^{\zeta} (1 - p_2 y^{\eta}) \right] , \tag{3.3-1}$$

$$q = q_o + q_1 \, y^{\lambda} + q_2 \, y^{\nu} , \qquad \text{or} \tag{3.3-2}$$

$$q = \frac{q_o}{(1 - \zeta \, y^{\rho})^{\sigma}} . \tag{3.3-3}$$

Here y is the poloidal flux normalized to 95% of the $\times$-point flux. In the pressure profile function, beta determines p_o, profiles are adjusted through p_1, and other variables are set according to $\alpha = 1.5$, $\gamma = 2.5$, $\zeta = 3$, $\eta = 1.2$, and $p_2 = 0$ or 1. For the safety-factor profile function of Eq. (3.3-2), $\lambda = 6$, $\nu = 2$, and q_o is chosen such that $q_{95} = q_o + q_1 + q_2 = 3.1$ (where q_1 and q_2 are independent variables). The safety factor profile function of Eq. (3.3-2) used for the case with $A \approx 6$, has $\sigma = ln(q_o/q_{95})/ln(1 - \zeta)$, $\zeta = 0.7$, and $\rho = 2$.

The shape of the 95% flux surface is given by

$$R = R_o + a \cos(\theta + \delta' \sin\theta) , \tag{3.3-4}$$

$$Z = \kappa_{95} \, a \sin\theta , \tag{3.3-5}$$

where $\delta' \approx \delta_{95}$. The 95% flux surface is used in the stability analysis to avoid the numerical difficulties near the $\times$-point.

The stability data base produced by the PEST code [7] is shown in Fig. 3.3-1 as the dependence of beta limit on κ_{95} (for $A \approx 6$) and as the dependence of Troyon factor [5]

limit, $C_T = \beta a B_t / I_p$ (in % Tm/MA), on A. From this result, one obtains

$$C_T \approx 2.8 \left[\frac{1 - 0.4(\kappa_{95} - 1)^2}{(1 - \epsilon)^{1.5}} \right], \tag{3.3-6}$$

which gives $C_T \approx 3.5$ and $\beta \approx 2.06\%$ for the reference plasma parameters in Table 3.2-III. It is important to note that this approximate scaling has a limited basis and its use should be limited to the profiles given here and to the range of parameters indicated above. For $A \approx 3$, it has also been shown that this beta limit remains relatively unchanged as long as l_i remains below 0.75.

Additional studies of the beta limit have also been carried out using polynomial profiles and with parameters encompassing the reference case: I_p ranging from 16 to 8 MA, q_{95} from 3 to 6, and β_p from 1.4 to 3. The value of C_T is 3.1 to 3.2 as long as q_{95} is above 3.7. This result is considered conservative relative to the preceding indications. Design values of $C_T = 3.2$ (corresponding to $\beta = 1.9\%$) and $l_i = 0.74$ are therefore adopted for the ARIES-I reactor.

3.3.2. Stability of Reference Equilibrium

To ensure complete self-consistency among MHD equilibrium and stability, current drive, and transport analysis, the ARIES-I reference equilibrium is found using a simple pressure function, $p(\psi) = p_o \tilde{\psi}^\alpha$, where $\alpha = 1.4$ and $\tilde{\psi}$ is the normalized poloidal flux. The equilibrium flux contours and profiles of safety factor and toroidal current density of the reference equilibrium are similar to those displayed in Figs. 3.2-2 and 3.2-3. As shown in Sec. 4, this equilibrium can be generated with ~100 MW of absorbed RF heating [mostly ion-cyclotron range-of-frequency (ICRF) fast-wave current drive]. The pressure profile also matches that of transport analyses.

Several sequences of equilibria were tested for stability at different aspect ratios and safety factors. In the range $4.5 \leq A \leq 6.0$, it was always possible to obtain stability at Troyon ratios $C_T \lesssim 3.2$. For the interim geometry of Table 3.2-III, stable equilibria were found in the range $1.56\% \leq \beta \leq 2.60\%$ as the axis safety factor varied respectively from $q_o = 1.50$ to 1.10. All equilibria were stable to $n = \infty$ ballooning modes (tested with the Phillips code [9]) and were stable to $n = 1$ external kinks (tested with PEST II) with the conducting wall at infinity. Generally the edge safety factor, q_a, was roughly four times the axis value, and it was found necessary to avoid integer values of q_a in order to ensure kink stability.

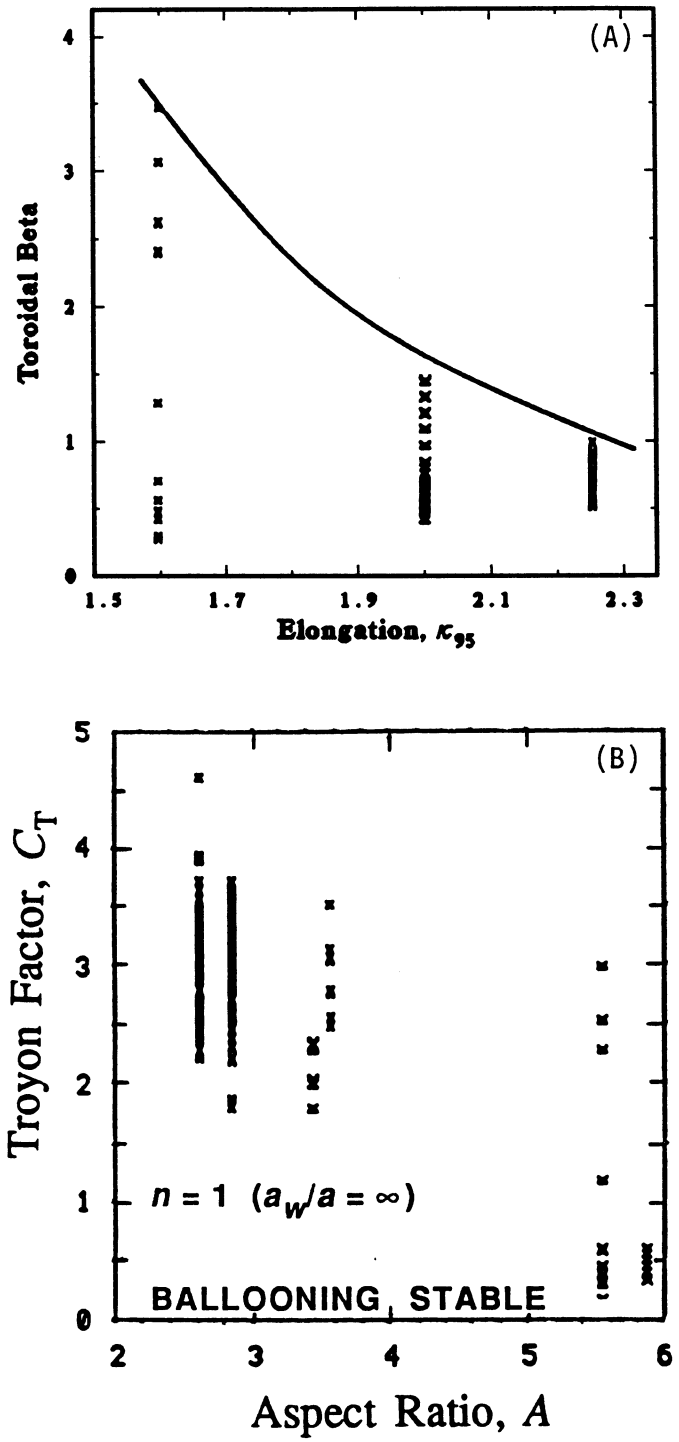

Figure 3.3-1. The stability data base produced by the PEST code [7]: (A) dependence of the beta limit on κ_{95} (for $A \approx 6$), and (B) dependence of the Troyon factor [5] limit, $C_T = \beta a B_t / I_p$ (in % Tm/MA), on the plasma aspect ratio, A.

3.4. VERTICAL STABILITY

Vertical stability is an important issue for ARIES-I because of the moderate-to-high aspect ratio ($A \geq 4.5$) and the high separatrix elongation ($\kappa_x = 1.8$). A toroidally continuous conducting shell is required to retard the growth of an externally excited vertical instability with a time constant ranging from an Alfvén time ($\tau_A \sim 10$ μs) without a shell to the electrical L/R time constant of the shell, $\tau_{L/R}$. The passive stabilization provided by this shell must be augmented by an active feedback system that provides vertical stability for times $\gtrsim \tau_{L/R}$. A rigid-plasma model (PSTAB) [10] and linear (NOVA-W) [11] and non-linear tokamak-simulation-code (TSC) [3] deformable-plasma models are used to estimate the conductor location and size required for passive stabilization. Time-dependent TSC simulations are used to determine the current, voltage, location and size of the feedback coils.

3.4.1. Passive Stabilization

Without passive stabilization, a vertically displaced plasma will move vertically on an Alfvén time scale ($\sim$10 μs). Passive conductors must be positioned around the plasma to slow this vertical motion sufficiently to allow an active feedback system operating on a longer time scale ($\gtrsim$ 100 ms) to control the vertical position of the plasma with a reasonable expenditure of reactive power ($\lesssim$ 10 MVA). Passive stability performance is measured by the stability parameter that is defined for an idealized system by

$$f \equiv 1 + \frac{\tau_v}{\tau_{L/R}}, \tag{3.4-1}$$

where $\tau_v = 1/\gamma$ is the vertical-instability time constant and γ is the growth rate. A design constraint of

$$f \geq 1.3, \tag{3.4-2}$$

is adopted to ensure that a sufficient stability margin exists above the $\gamma = \infty$ limit under all plasma conditions.

Placement of passive (metallic) stabilizer elements close to the plasma cause severe engineering difficulties: (1) neutron damage and activation, (2) nuclear heating which requires active cooling, (3) adverse effects of tritium breeding, and (4) difficulties in assembly/disassembly of components and of maintenance. It is, therefore, desirable to place the passive elements away from the plasma, preferably behind the blanket (at a

distance of $\sim 0.6a$ from the plasma surface in ARIES-I). A preliminary analysis of the maximum allowable distance permitted between the plasma and the passive stabilizer elements for vertical stability was performed with the PSTAB [10] code. The PSTAB formulation assumes that the plasma is a massless rigid body simulated by an array of filamentary current elements. The equations describing a small vertical displacement in the presence of an array of resistive filamentary conductors simulating the passive stabilizer are linearized and solved as an eigenvalue problem.

The notation used to describe the location of the passive stabilizer relative to the plasma is shown in Fig. 3.4-1. The plasma surface is assumed to be given by

$$Z = a\kappa_x \sin\theta\,, \tag{3.4-3}$$

$$R = R_o + a\cos(\theta + \delta_x \sin\theta)\,, \tag{3.4-4}$$

where R_o is the major radius, a is the minor radius, κ_x and δ_x are, respectively, the separatrix elongation and triangularity, and the poloidal angle θ varies from 0 to 2π. The passive stabilizer is placed on a surface parallel to the plasma surface.

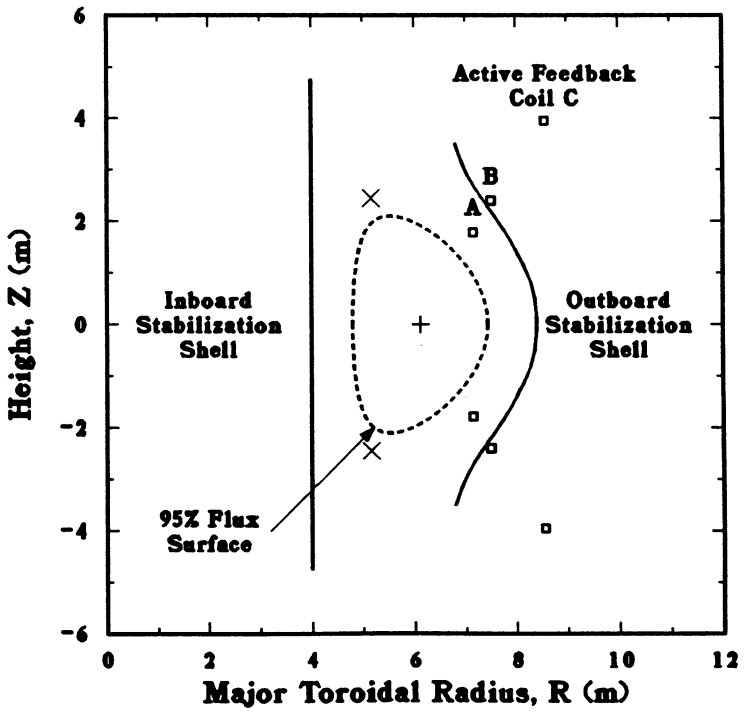

Figure 3.4-1. The geometry of the plasma and the passive stabilizer (shell).

A series of calculations were performed for an $A = 6$ plasma that was considered during the ARIES-I scoping-phase activities ($R_o = 6$ m, $a = 1$ m, $\kappa_x = 2$, $\delta_x = 0.5$). The poloidal coverage, p/a, and the normalized radial location, c/a, of a passive outboard stabilizer were varied and the results are shown in Fig. 3.4-2. It was found that relatively small passive stabilizers ($p/a \sim 0.2$) meet the stability constraint, but these conductors must be located close to the plasma ($c/a \leq 1.1$). Placement of the passive stabilizer behind the blanket (0.9 m away from plasma surface), even with full coverage on the outboard side, does not provide sufficient stabilization (*i.e.*, $f > 1.3$).

The cost-optimized ARIES-I design, however, has a lower aspect ratio of $A = 4.5$. Vertical stability of $A = 4.5$ plasmas with passive stabilizer elements positioned behind the blanket, as shown in Fig. 3.4-3 (0.7 m away from the plasma surface on the inboard side and 0.9 m on the outboard side) were examined. The stability parameter as a function of the plasma elongation of such plasmas is shown in Fig. 3.4-4. This analysis indicates that $\kappa_x \lesssim 1.83$ is required for a stabilizer located behind the inboard and outboard blankets.

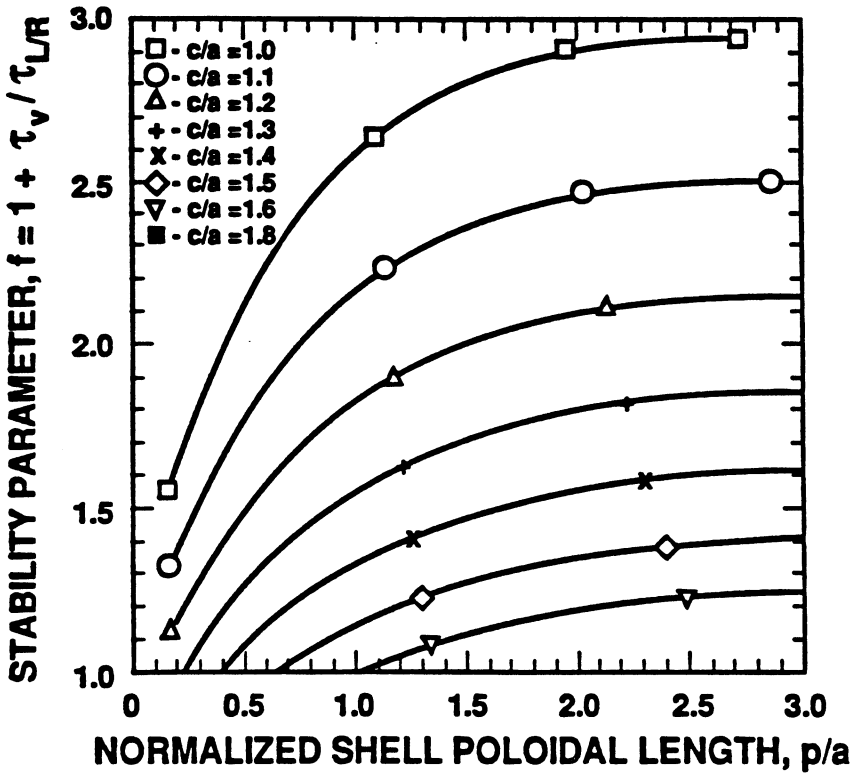

Figure 3.4-2. The stability parameter as a function of poloidal coverage of an outboard stabilizer at various radial locations (c/a) (Fig. 3.4-1) for $A = 6$, $\kappa_x = 2$, and $\delta_x = 0.5$.

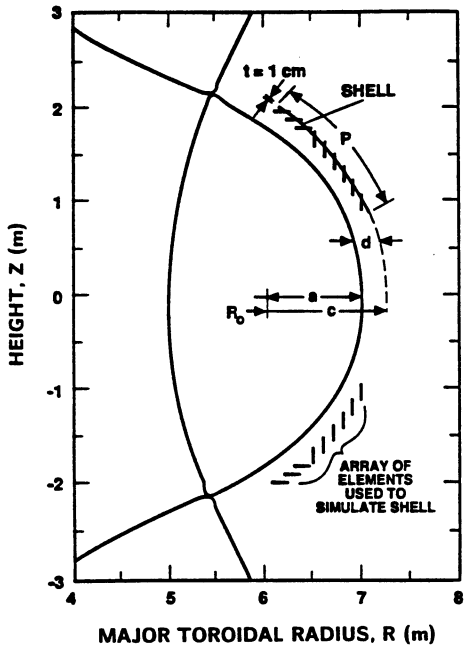

Figure 3.4-3. The geometry of the plasma and the passive stabilizer for $A = 4.5$ and $\kappa_x = 1.74$. A similar geometry was used for the other cases in the κ parametric study. The coil locations used in the active feedback analysis are also indicated.

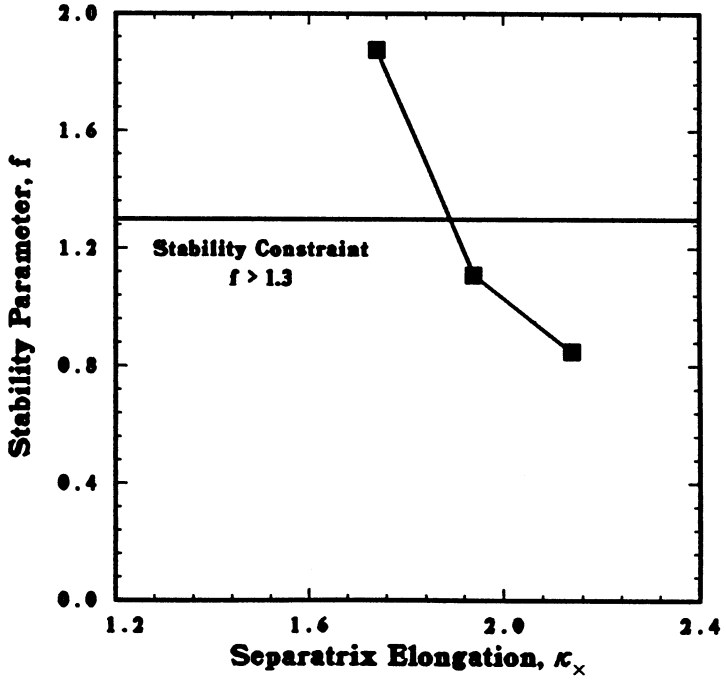

Figure 3.4-4. Dependence of the stability parameter on elongation for $A = 4.5$ and stabilizer geometry shown in Fig. 3.4-3.

The accuracy of the PSTAB rigid-plasma model results was then checked by benchmarking the $\kappa_X = 1.74$ case against the TSC and NOVA-W deformable-plasma models. The TSC [3] performs time-dependent simulations of resistive free-boundary, axisymmetric plasmas and the associated external conductors and poloidal-field circuits, including active feedback amplifiers. Consequently, TSC is more costly to use than either PSTAB or NOVA-W. The plasma force balance in TSC is modified by scaling up the plasma mass and viscosity to maintain the plasma in force balance, while alleviating the time-scale disparity between wave and diffusion phenomena. This parameter scaling does not affect plasma bulk motion that is stable on the ideal-MHD time scale (μs), but does affect the growth rate of vertical instability. To calculate τ_v, TSC is set up with the plasma and passive-stabilizer geometry shown in Fig. 3.4-3. The PF coils are represented with a multipole series truncated with the even decapole. The simulations begin with a radial magnetic field applied for 1 μs to produce an initial ~3-mm vertical displacement of the plasma. The plasma simulation is then continued until the equilibrium effects of the initial perturbation are damped out and the vertical instability asymptotically relaxes to a linear growth rate, as reported by inboard and outboard pickup coils. Corroboration of the value of τ_v predicted from the pickup coils was obtained by fitting the vertical displacement of the magnetic axis, Z_M, with the functional form,

$$Z_M(t) = Z_o\, e^{t/\tau_v} . \tag{3.4-5}$$

This τ_v calculation was made for four values of plasma mass-enhancement factors. Results (denoted as squares) are shown in Fig. 3.4-5. An analytically derived quadratic polynomial that yields the behavior of τ as a function of the plasma mass-enhancement factor for small values of the mass-enhancement factor was fit to the results and then extrapolated to a unity mass-enhancement factor to determine the mass independent value of τ_v reported in Table 3.4-I. The accuracy of this extrapolation is demonstrated by fitting polynomials to the three smallest and three largest mass-enhancement-factor results displayed in Fig. 3.4-5 and reporting a range for τ_v and f in Table 3.4-I.

This calculation was repeated with the NOVA-W code [11], a non-ideal MHD linear-stability code that was developed to calculate the linear stability of axisymmetric modes with passive resistive conductors and active feedback included in the vacuum region surrounding the plasma. The NOVA-W code is a derivative of the NOVA [12] code. Both codes are non-variational MHD stability codes that solve the stability eigenvalue problem for the growth rate (eigenvalue). The use of the eigenvalue formulation rather than the δW formulation to calculate stability permits the inclusion in NOVA-W of non-ideal effects, such as wall resistivity, that would otherwise destroy the self-adjointness

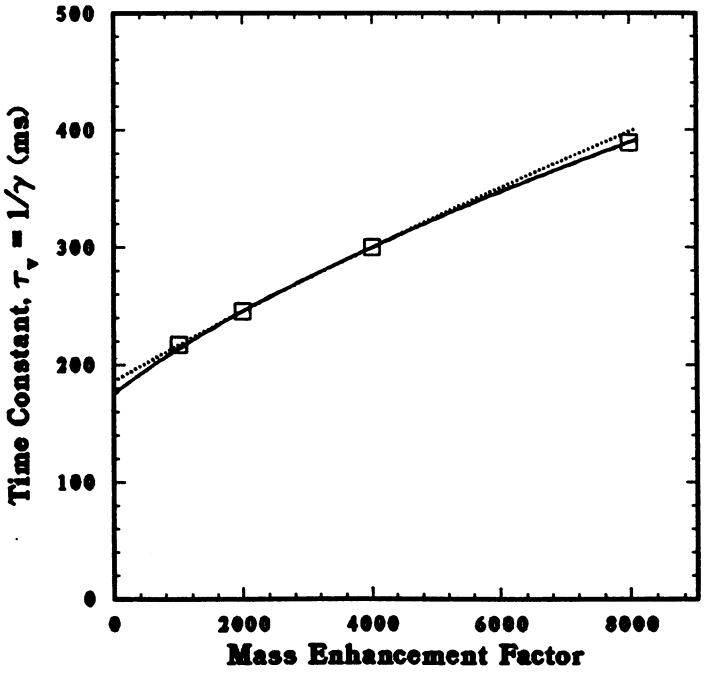

Figure 3.4-5. Dependence of the vertical-stability time constant on plasma mass-enhancement factor as calculated with TSC (squares) for $A = 4.5$, $\kappa_x = 1.74$, and the stabilizer geometry shown in Fig. 3.4-3. Also included are quadratic polynomials fitted to the three largest (solid) and three smallest (dash) mass-enhancement-factor results and extrapolated to a unity mass-enhancement factor.

Table 3.4-I.
Vertical Stability Benchmark of the Configuration Shown in Fig. 3.4-3

Code	Vertical-Stability Time Constant, τ_v (ms)	Stability Parameter, f
PSTAB [10]	217	1.88
TSC [3]	175 – 186	1.56 – 1.60
NOVA-W [11]	173	1.55

property underlying the δW approach. A Green's function formulation is used to express the perturbed poloidal flux in the vacuum region in terms of the feedback currents in the vacuum region and an integral over the boundary surfaces: the plasma/vacuum interface and the surface of the resistive wall surrounding the plasma. Separate Green's equations are obtained for the vacuum region between the plasma and the resistive wall, and for the region outside the resistive wall. A thin wall approximation is used to relate the discontinuity in the normal derivative of the poloidal flux across the thin resistive wall boundary to the time derivative of the flux on the boundary. Combining the Green's equations for the different boundary surfaces yields the normal derivative of the perturbed flux at the boundary in terms of poloidal flux, which in turn is known as a function of the Fourier modes of the displacement. This approach provides the correct vacuum boundary condition needed to solve the NOVA eigenvalue equation for the growth rate and eigenfunction of the instability. An ARIES-I equilibrium produced with TSC is used as input to the NOVA-W code. Special care must be used for equilibria (such as those of ARIES-I) where the separatrix is near the plasma surface, because this condition can adversely affect the accuracy of the mapping to stability coordinates and, therefore, affect the result. Consequently, equilibria limited by the 95% flux surface and below are used in the NOVA-W calculation and then the growth rates are extrapolated to the separatrix. The NOVA-W result for the benchmark case is given in Table 3.4-I. Agreement between the NOVA-W result and the mean TSC result is good at 4% for τ_v and 2% for f, but agreement between the PSTAB result and the mean TSC result is 20% for τ_v and 19% for f. The differences between PSTAB and TSC result in part from rigid-*versus* deformable-plasma effects and from differences in the calculation of the stabilizer inductances. Also, a 20% difference was obtained in the PSTAB and TSC calculations of $\tau_{L/R}$ with a vertically asymmetric current distribution in the stabilizer.

The possibility of placing the passive stabilizer behind the shield and effectively using the vacuum vessel as the stabilizer element was also considered. To examine the feasibility of such a move, NOVA-W was used to analyze a 0.01-m-thick aluminum ($\eta = 2.824 \times 10^{-8}$ Ω-m) stabilizer shell located either behind the blanket (inner wall configuration) or behind the shield (outer wall configuration) as shown in Fig. 3.4-6. The results indicate that the growth time for the axisymmetric mode for the inner wall configuration is 330 ± 5 ms. For the outer wall configuration, the growth time is 44 ± 1 ms. In fact, the outer wall configuration was found to be unacceptably close to the ideal stability limit, having a stability parameter $f < 1.1$. Therefore, only the inner vacuum-vessel wall configuration is effective in stabilizing the axisymmetric mode to a time scale that an active feedback system can handle with reasonable power levels.

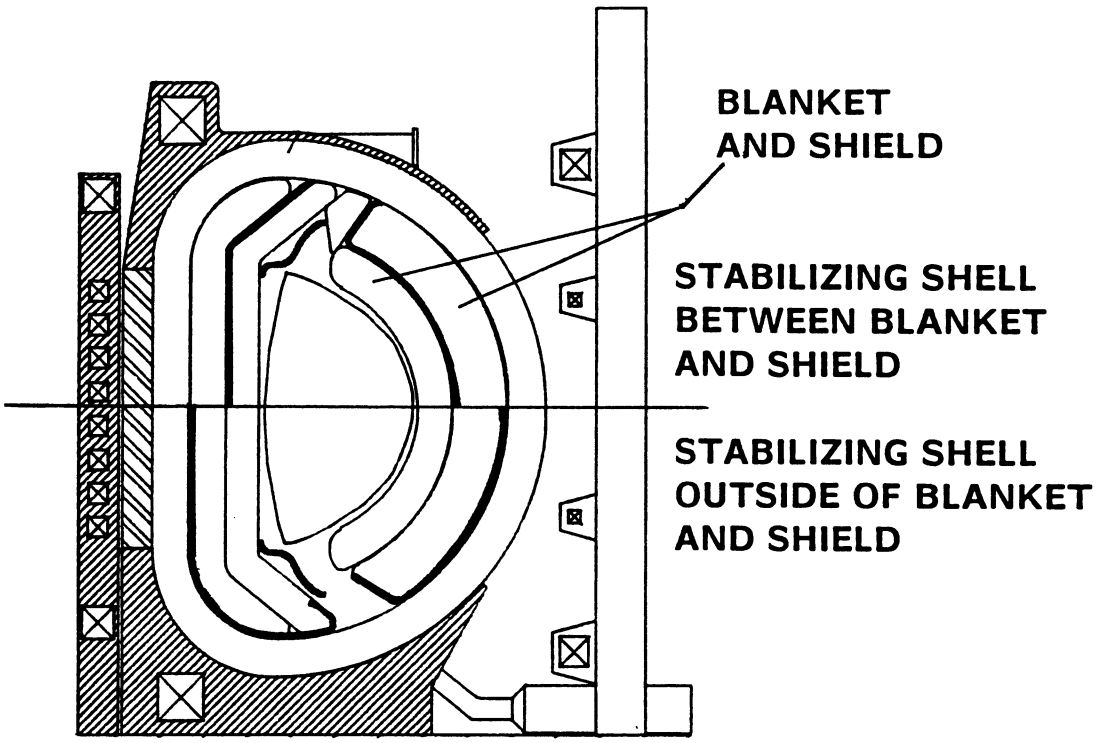

Figure 3.4-6. The geometry of two possible locations for passive stabilization shells considered: behind the blanket (inner location) and behind the shield (outer location). The effect of tungsten divertor plates was included in both cases.

3.4.2. Active Feedback

The active-feedback power requirements were determined from TSC simulations of the $A = 4.5$ and $\kappa_X = 1.74$ case used in the passive stability benchmark described in the Sec. 3.4.1. A simulation begins with the vertical coordinates of the plasma magnetic axis, Z_M, maintained in the equatorial plane for 0.1 s. The feedback coils are pre-programmed to initiate a 50-mm vertical displacement of Z_M at 0.1 s into the simulation and to maintain that position once attained. As the plasma mass does not affect the voltage or current of the feedback coils, a large mass-enhancement factor (8,000) was used for computational expediency.

Simulation results for feedback-coil A (Fig. 3.4-3) are given in Fig. 3.4-7. A gain for driving the feedback-coil current was selected to yield a common value of $G \sim -2.6$ for the dimensionless gain defined as the ratio of the response flux difference produced by the feedback coils to the flux difference produced by the plasma in the pickup coils. The dimensionless gain must be in the range of -1 to -10 to ensure stability and practicality

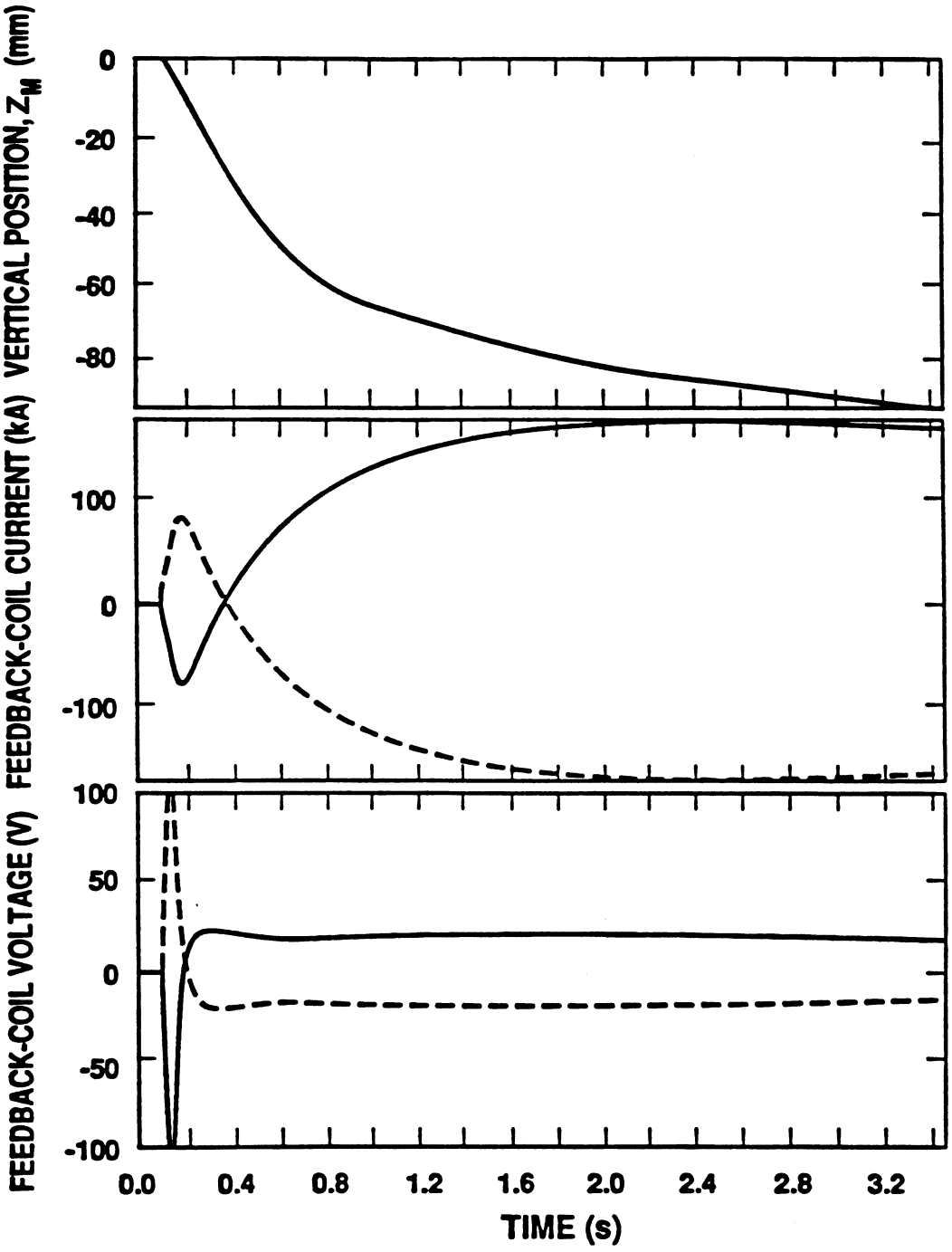

Figure 3.4-7. The vertical position of the magnetic axis and the feedback-coil current and voltage as functions of time as calculated with TSC for $A = 4.5$, $\kappa_x = 1.74$, the stabilizer geometry shown in Fig. 3.4-3, and feedback-coil A in Fig. 3.4-3.

of the feedback system. A value of $G \sim -2.6$ rapidly moves the plasma to a 50-mm displacement with only an ~10-mm overshoot. The gain for driving the feedback-coil voltage is set at a low value of 1 mV/A to ensure a smooth voltage response. A pickup-coil location approximately equal to the location of feedback-coil B in Fig. 3.4-3 was used for feedback-coils A and C. For feedback-coil B, a pickup-coil location corresponding approximately to the location of feedback-coil A was used to obtain a clear resolution of the flux difference produced by the plasma.

The maximum reactive power occurs at the maximum vertical displacement of Z_M and scales with Z_M^2. The reactive power requirements for the three feedback-coil locations of Fig. 3.4-3 are shown in Fig. 3.4-8 for a common 50-mm displacement of Z_M. The feedback coils were simulated with a 0.1-m × 0.1-m cross section of room-temperature, copper alloy with a conductor filling fraction of 0.7. Feedback-coil C is preferable over the other two coil locations. This coil is positioned just outside of the TF coil and is easily accessible for maintenance. The ~2 MVA reactive power required to drive this coil is well within the 26 MW of recirculating power set aside for miscellaneous plant needs (Sec. 2). Furthermore, a 50-mm displacement could not be tolerated by the divertor and represents a maximum design constraint.

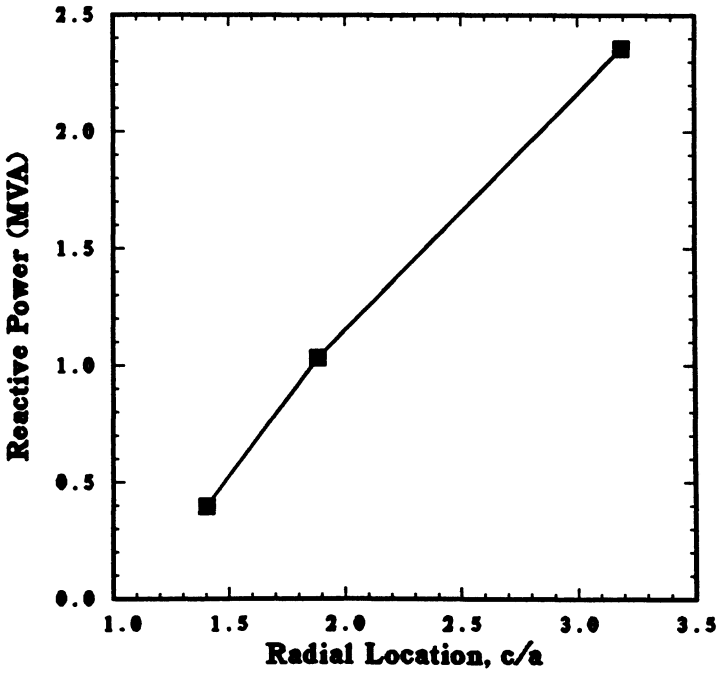

Figure 3.4-8. The reactive power as a function of normalized radial location calculated with TSC for $A = 4.5$, $\kappa_X = 1.74$, and the geometry shown in Fig. 3.4-3. Simulation results were scaled to a common 50-mm displacement of Z_M.

3.5. TRANSPORT ANALYSIS

The 1-1/2-D, time-dependent BALDUR transport code [13] was used to simulate steady-state core-plasma behavior for the ARIES-I tokamak design and to study the time evolution of plasma density and temperature from a few keV (*i.e.*, typical of ohmic discharges) to a steady-state fusion plasma. In addition to the analyses of the approach to ignition and thermal stability, the BALDUR simulations were used to study fueling of the ARIES-I plasma, the resultant density and temperature profiles, and helium ash buildup and exhaust. The parameters of the steady-state ARIES-I plasma were also used to benchmark the 0-D results of the systems code. Several physics models including an estimate for synchrotron radiation losses (Sec. 3.5.1) and transport models (Sec. 3.5.2) were incorporated in BALDUR for ARIES-I transport analyses which are reported in this section.

In addition to BALDUR simulations, the ARIES-I reference equilibrium with the simple pressure profile of $p(\psi) = p_o\tilde{\psi}^{\alpha}$ ($\alpha = 1.4$ and $\tilde{\psi}$ is the normalized poloidal flux), was used to calculate and benchmark the ARIES-I fusion-power performance and operating point. The 2-D flux contours for this equilibrium were used in the TRAC II code, which computes a flux-surface-averaged power balance. This study was performed to ensure complete self-consistency among all plasma physics analyses since the density and temperature profiles used in this power balance analysis are exactly the same as those used for the current-drive and stability calculations, and these profiles are roughly consistent with the BALDUR results (although the 1-D BALDUR transport calculation cannot be exactly compared to 2-D MHD profiles).

The plasma profiles used include a peaked temperature profile, $T_e(\psi) = T_{eo}\tilde{\psi}^{\alpha_T}$, with $\alpha_T = 1.1$ and $T_{eo} = 44$ keV, and a broad density profile, $n_e(\tilde{\psi}) = n_{eo}\tilde{\psi}^{\alpha_n}$, with $\alpha_n = 0.3$ and $n_{eo} = 1.85 \times 10^{20}$ m^{-3}. The profile factors, α_T and α_n, were chosen so that the profiles are consistent with BALDUR simulations and T_{eo} and n_{eo} are set so that the average temperatures and density agree with the systems code results. The alpha density was set at 10% of the fuel ions, and an additional (nominally oxygen) impurity was added to raise Z_{eff} to 1.6. The results of this simulation for the interim ARIES-I design point are summarized in Table 3.5-I and are in good agreement with systems code results and BALDUR simulations for that design point.

Table 3.5-I.
TRAC II Simulation of Interim ARIES-I Parameters

Major toroidal radius, R_o (m)	7.245
Minor radius (95%), a (m)	1.555
Elongation, κ_{95}	1.60
Triangularity, δ_{95}	0.50
Plasma volume (95%) (m^3)	523
Shape factor, S	1.33
Approximate first-wall area (m^2)	629
Plasma current, I_p (MA)	10.6
On-axis toroidal field, B_t (T)	11.6
Toroidal beta, β (%)	1.9
Troyon coefficient, C_T (% Tm/MA)	3.2
RMS beta, β^* (%)	2.52
Shafranov poloidal beta, β_I	2.4
On-axis safety factor, q_o	1.3
Toroidal radius of magnetic axis, R_m (m)	7.481
Self-inductance, L (μH)	17.3
Plasma pressure (MPA)	
Peak, p_o	2.97
Volume averaged, $\bar{p}$	1.03
Electron temperature (keV)	
Peak, T_{eo}	44.2
Volume averaged, $\bar{T}_e$	17.4
Electron density (10^{20} m^{-3})	
Peak, n_{eo}	1.85
Volume averaged, $\bar{n}_e$	1.33
Fuel-ion density (10^{20} m^{-3})	
Peak, n_{DTo}	1.44
Volume averaged, $\bar{n_{DT}}$	1.04
Effective plasma charge, Z_{eff} (~1% oxygen)	1.6
Absorbed current-drive power, P_{CD} (MW)	100
Fusion power, P_f (MW)	2,100
Average neutron wall load (MW/m^2)	2.7

3.5.1. Synchrotron Radiation Effects

A unique feature of the ARIES-I reactor is that half of the plasma energy is radiated in the form of synchrotron radiation. The synchrotron power is high because: (1) the first-wall material is SiC composite which is poorly reflective, (2) high on-axis magnetic field, and (3) high electron temperature. A large synchrotron radiation is beneficial because the heat load to the divertor plates will be reduced. On other hand, a better core-plasma confinement (conduction and convection) is required.

To determine the synchrotron radiation losses, the overall reflectivity of the first wall should be calculated. The first wall of ARIES-I comprises an SiC-fiber composite shell coated with a 2-mm-thick chemical-vapor-deposited SiC layer (Sec. 8). Helium coolant flows through channels inside the shell. A mixture of Li_2ZrO_3 solid breeder and Be multiplier in the form of sphere-pac is located behind the first wall. The spectrum of synchrotron radiation emitted from the plasma peaks at the fifth electron-cyclotron harmonic ($\sim$1.64 THz) and extends all the way to the far infrared regime, but short of the regions of resonant and relaxation absorption by either He gas or SiC. Dissipation of the radiated power, therefore, takes place solely as a consequence of the presence of charge carriers in the SiC molecules due to gamma irradiation or the introduction of elemental impurities (*e.g.*, Be, B, and Aℓ), which results in a finite electrical conductivity. Data on the electrical properties of SiC are limited, but millimeter wave measurement on water-free fused silica, for example, shows a loss tangent value of 10^{-3} at $\sim$400 GHz [14]. The value of the loss tangent is a sensitive function of both frequency of the radiation and purity of the material (see also Sec. 4.5.3).

Using a multi-slab model of the first wall and assuming a loss tangent in the range of 5×10^{-3} to 0.1 for SiC composite (corresponding to an equivalent conductivity of 5 to 100 mhos/m), the effective reflectivity of SiC-composite first wall is calculated to be 0.27. The divertor target plates of ARIES-I are coated with tungsten which has an effective reflectivity of 0.99. Noting that the divertor-plates cover 20% of the total first-wall area, the overall first-wall reflectivity, $\Re$, has been found to be 0.41.

There are many ways to calculate the total synchrotron-power radiated from the plasma given its density and temperature profiles [15]. The most rigorous approach is to solve the equation of radiative transfer in an inhomogeneous plasma, taking into account the emission, re-absorption, reflection from the wall, and transport of the radiation within the plasma. This problem was already solved by Tamor and the results are embodied in the SNECTR code [16]. Subsequently, a much simpler and less time-consuming code, CYTRAN, was developed [17] and satisfactorily benchmarked against SNECTR.

For ARIES-I applications, where a weakly reflecting wall is required, a calculational method simpler than using CYTRAN is possible. It involves the local application of the global model (LAGM) of synchrotron power loss from a homogeneous, cylindrical plasma at each point inside an inhomogeneous plasma. This so-called LAGM method was first proposed by Tamor [18] and was found to give total power loss, and associated radial cooling profiles, in reasonable agreement with those of SNECTR, particularly when the wall is weakly reflecting ($\Re \ll 1$).

Using Trubnikov's approach [19] and including the relativistic correction factor, the local radiated-power density is given by:

$$W_{sync} = 4.14 \times 10^{-11}(1-\Re)^{1/2} n_e^{1/2} T_e^{5/2} B_t^{5/2} (1-\beta)^{5/4} \times a^{-1/2} \kappa^{-1/4} \left(1 + \frac{T_e}{204}\right) \left(1 + \frac{18a\,\kappa^{1/2}}{R_o\, T_e^{1/2}}\right)^{1/2}, \qquad (3.5\text{-}1)$$

where SI units are used except for the electron temperature, T_e, which is in keV. Also, n_e is the electron density, B_t is the magnetic field strength, β is the plasma beta, κ is the plasma elongation, R_o is the major radius, and a is the minor radius. The expression in Eq. (3.5-1) can be integrated over the plasma density and temperature profiles to obtain the total synchrotron-power loss, P_{sync}.

To check the accuracy of the LAGM calculation of the W_{sync} profile, the reference ARIES-I parameters of Table 3.1-I were used for benchmarking against the results of CYTRAN. Shown in Fig. 3.5-1 are the radiated-power density profiles as a function of normalized plasma radius, calculated by LAGM using Eq. (3.5-1) and by CYTRAN. The corresponding total radiated powers, P_{sync}, are 303 MW and 266 MW for, respectively, LAGM and CYTRAN, which compare reasonably well with the value of 221 MW calculated from the systems code. It is noted from Fig. 3.5-1 that the two profiles have very similar radial dependence, except for the difference in their local magnitudes that accounts for the 14% difference in P_{sync}. At $\Re = 0.41$, W_{sync} from CYTRAN shows a small negative value near the plasma periphery, implying net synchrotron heating due to reabsorption of the wall-reflected synchrotron power. This effect, of course, is not taken into account by the LAGM calculations.

It should be pointed out here that W_{sync}, as calculated from Eq. (3.5-2), scales as $n_e^{1/2} T_e^{5/2} B^{5/2}$ and, therefore, is strongly sensitive to the electron temperature profile and the magnetic field. In addition, since P_{sync} and the alpha heating power have the same order of magnitude in ARIES-I, an accurate evaluation of the W_{sync} profile and P_{sync} is essential in determining the self-consistent n_e and T_e profiles, and the plasma thermal

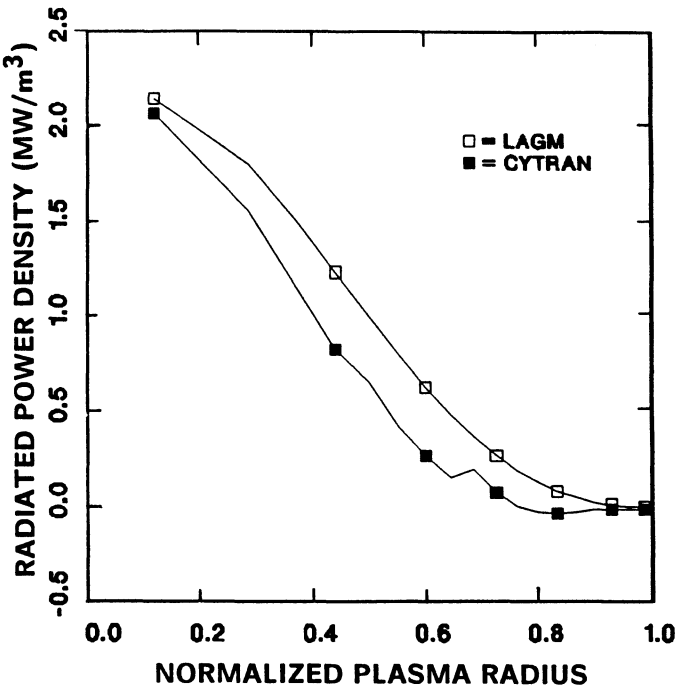

Figure 3.5-1. Radial profiles of synchrotron radiated-power density calculated by LAGM using Eq. (3.5-1) and by CYTRAN, for the reference ARIES-I parameters.

equilibrium point. For this reason, the LAGM calculation of W_{sync} in conjunction with Eq. (3.5-1) is incorporated into the 1-D BALDUR transport code, which will be discussed in the following sections.

3.5.2. The ARIES-I Transport Model

The transport model that was implemented in the BALDUR transport code was adapted from Houlberg's plasma modeling work on the compact ignition torus [20]. This model is purely empirical and is designed to reproduce the global empirical scalings of energy and particle confinement time. In addition to global agreement with empirical scalings, this model has been used successfully at the Princeton Plasma Physics Laboratory to predict the density and temperature profiles in certain pellet-fueled TFTR discharges [21]. Houlberg has also been successful in predicting plasma density and temperature behavior on JET discharges using this transport model in the WHIST transport code [20].

The Houlberg transport model is based on the following assumptions: (1) The radial ion and electron thermal diffusivities are equal. (2) The radial particle-diffusion coef-

ficient, $D_\perp$, is equal to 1/2 the radial thermal diffusivity, $\chi_\perp$. (3) The edge thermal diffusivity is five times that at the center. (4) There exists an anomalous inward particle pinch for ions and electrons proportional to the particle diffusion coefficient. The radial thermal diffusivity, $\chi_\perp(r)$, is defined as

$$\chi_\perp = \frac{a^2}{4\tau_E}\left(1+\frac{4r^2}{a^2}\right)\left(\frac{2\kappa^2}{1+\kappa^2}\right) C_N\,, \tag{3.5-2}$$

where a is the plasma minor radius, κ is the plasma vertical elongation, r is the radial plasma coordinate, C_N is a normalizing factor equal to 0.218, and τ_E is the global diffusive energy-confinement time. For ARIES-I simulations, τ_E is assumed to scale as the empirical Riedel-Kaye energy-confinement time [22],

$$\tau_{E,R-K} = 0.03\, f_H\, a^{-0.27} R_o^{1.64} I_p^{1.01} B_t^{0.07} n^{-0.04} P^{-0.54} \kappa^{0.59} A_i^{0.5}\,, \tag{3.5-3}$$

where f_H is the confinement enhancement factor over the so-called L-mode, R_o is the major toroidal radius, I_p is the plasma current, n is the electron density, and P is the net plasma-heating power (assumed to be equal to total plasma-heating power minus the radiation losses). In Eq. (3.5-3), SI units are used except for I_p in MA, n in 10^{19} m^{-3}, and P in MW. The confinement enhancement factor, $f_H = 2.8$, was used in the BALDUR simulations.

The anomalous inward particle pinch has been introduced by Stotler as a refinement on Houlberg's transport model to give improved agreement between BALDUR simulations and TFTR discharges in terms of density profiles. This inward pinch is given as [21]

$$V_{pinch} = -\frac{2\,D_\perp\, r}{a^2}\,. \tag{3.5-4}$$

For the ARIES-I simulation work, 3/4 of this pinch is included in the transport model. This choice was based on the fact that the difference between including the full pinch and 3/4 of the pinch was less than the scatter in the empirical data base on which the transport model had been benchmarked. Therefore, there was some freedom in choosing the exact multiplying factor for the inward pinch and the lower value of the inward pinch was used.

In the simulation of the ARIES-I plasma, the MHD equilibrium was determined by solving the Grad-Shafranov equation in two dimensions. The 2-D grid used to solve this differential equation was established by specifying a fixed boundary for the poloidal flux using the technique of harmonic moments [23]. The Grad-Shafranov equation was solved

every five seconds during the simulation using the evolving pressure and current-density profiles. As a result, the simulation involved a coupled evolution of 1-D radial transport and 2-D MHD equilibrium.

A high-n ballooning-mode transport model was included in the simulation to maintain the pressure gradient at or below the critical limit for the onset of ballooning modes. The transport model for ballooning modes is in the form of an enhancement factor, f_χ, on the local $\chi_\perp$ equal to [23]

$$f_\chi = \left[1 + A\left(\frac{p'}{p'_{crit}}\right)\right]^B , \tag{3.5-5}$$

where p' is the local pressure gradient, p'_{crit} is the pressure gradient limit for high-n ballooning modes, and values of $A = 1$ and $B = 10$ were used. The result of including this enhancement in $\chi_\perp$ is the local flattening of the temperature profile in regions where $p' > p'_{crit}$. In the ARIES-I plasma simulation, the effect of including this enhancement factor on global confinement time and the average temperature is found to be small. This result also confirms that the ARIES-I plasma is stable against high-n ballooning modes in the bulk of the plasma.

3.5.3. Transport Simulation Results

The transport models described in Secs. 3.5.1 and 3.5.2 were incorporated into the BALDUR code. The evolution of the ARIES-I plasma was simulated by starting with an ohmic-like plasma with a temperature of 5 keV on axis (typical of plasmas in ohmic equilibrium [24]) and continuing to steady-state, fusion-burn conditions. For ARIES-I simulations, it was assumed that the density and temperature profiles have pedestal boundary conditions such that at steady state $T_e(a) = T_i(a) = 0.30$ keV and $n_e(a) = 1.0 \times 10^{20}$ m^{-3}, where $T_e(a)$ and $T_i(a)$ are, respectively, the separatrix electron and ion temperatures, and $n_e(a)$ is the separatrix electron density.

The fast-wave current-drive system was used to heat the ARIES-I plasma to ignition. It was assumed that the auxiliary heating associated with the fast-wave current drive has a parabolic profile (consistent with the current-drive calculations of fast-wave power absorption in the plasma). The 96.7 MW of auxiliary heating is divided so that 93% of the power is delivered to electrons and 7% to the ions. The available current drive was found to be more than adequate for heating the ARIES-I plasma to ignition. Typically, the ARIES-I plasma achieved ignition in about 5 s and steady state in approximately

20 s of plasma simulation time; it maintained a steady burn for the remaining 20 s of the simulation.

The reference fueling scenario for the ARIES-I plasma includes the injection of 2-mm-radius pellets made of a 50:50 deuterium-tritium (DT) mixture at a frequency of 3 Hz. The pellets are injected at the mid-plane. In general, it was found that for the range of pellet size and speed considered, pellets would ablate in the outer 1/3 to 1/2 of the plasma radius (corresponding to pellet speeds of 5 and 20 km/s, respectively). In the simulations, the pellet fuel ions were transported towards the center by the anomalous inward particle pinch. The density profile was found to be very broad and, without an anomalous pinch term, the density profile would have been even flatter. On the other hand, the ARIES-I plasma was found to be very stable (thermal and MHD) to perturbations in the density profile. For example, Fig. 3.5-2 shows the evolution of temperature and density profiles of the ARIES-I plasma fueled with large size (4-mm radius) pellets injected every eight seconds. In this simulation, the density and temperature profiles were recovered in about 2 s after each pellet injection.

The transport simulation of the ARIES-I plasma gives a ^{4}He particle-confinement time of approximately 7.76 s. The ^{4}He ash buildup in steady state is 8.6%. This particle confinement is very sensitive to the value of the particle diffusion coefficient and to the inward pinch that is assumed in the simulation. It should be noted, however, that the assumption of $D_\perp = 0.5\chi_\perp$ and $V_{pinch} = -1.5\, D\, r/a^2$ results in plasma-core τ_P/τ_E values that are in the empirical range for present-day tokamak experiments.

The steady-state plasma-parameter values from the BALDUR simulations are compared to 0-D prediction of the systems code in Table 3.5-II. Good agreement between the 0- and 1-D values for the ARIES-I plasma parameters were found. The plasma pressure and density profiles are found to scale roughly as

$$p(r) = p_o \left[1 - \left(\frac{r}{a}\right)^2\right]^{\alpha_p}, \tag{3.5-6}$$

$$n(r) = n(a) + n_o \left[1 - \left(\frac{r}{a}\right)^2\right]^{\alpha_n}, \tag{3.5-7}$$

with $\alpha_p \simeq 1.4$ and $\alpha_n \simeq 0.3$. These profiles were used in other plasma analyses. The electron and ion temperature profiles however are not similar, the electron temperature being flatter than that of the ions. This difference in the temperature profiles is attributed to the flattening of the electron temperature profile due to a more accurate synchrotron-radiation model in the simulation (Sec. 3.5.1).

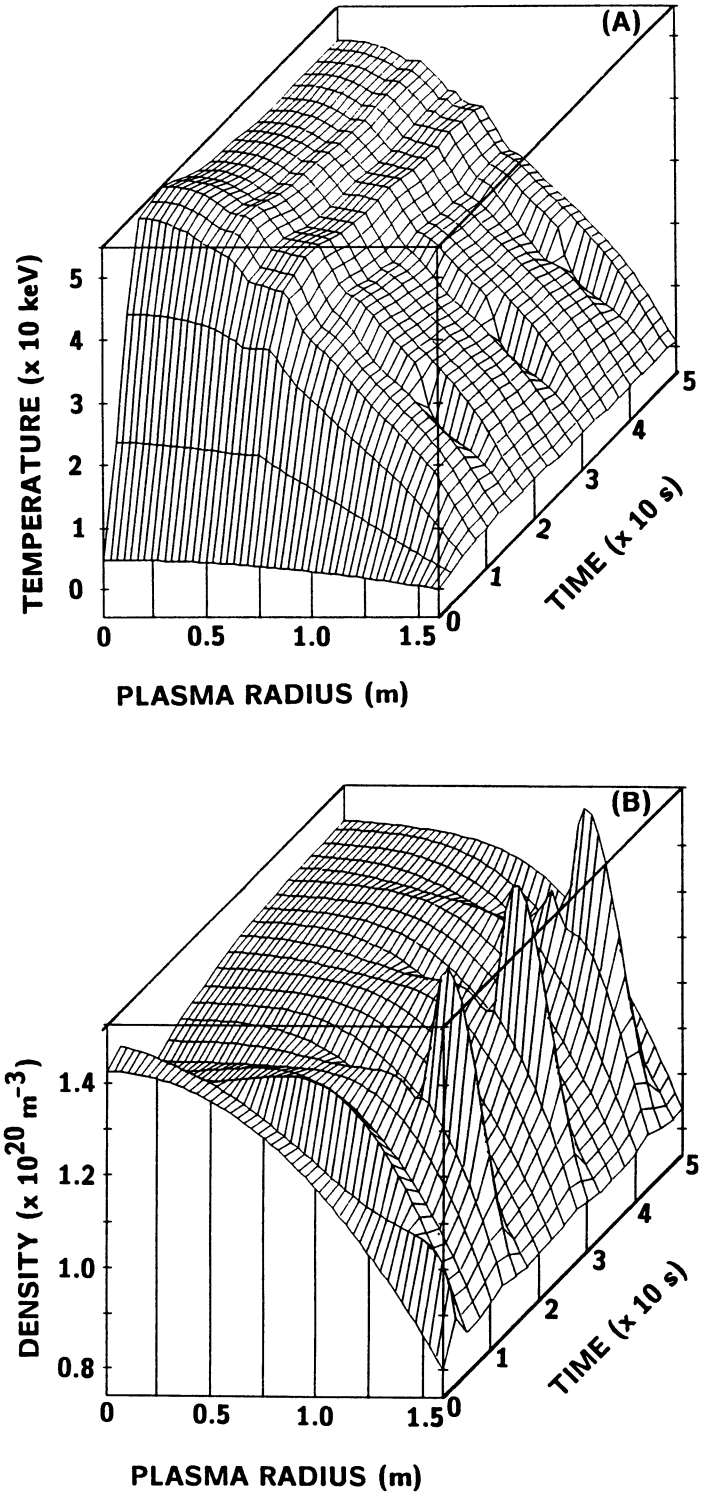

Figure 3.5-2. Time evolution of the ion (A) temperature and (B) density profiles.

Table 3.5-II.
Comparison of BALDUR Simulation Results with 0-D Predictions for ARIES-I Plasma Parameters

Plasma Parameters	BALDUR	0-D Simulations
Current-drive power (MW)	97.	97.
Alpha power (MW)	375.	385.
Energy confinement time (s)	2.49	2.53
Confinement enhancement factor, $f_{H,Riedel-Kaye}$	2.80	2.52
Particle confinement time (s)	7.76	9.39
Average electron density (10^{20} m^{-3})	1.39	1.45
Average ion density (10^{20} m^{-3})	1.20	1.24
Average electron temperature[a] (keV)	18.3	19.3
Average ion temperature[a] (keV)	20.7	20.0
Toroidal beta (%)	2.00	1.90
Effective plasma charge, Z_{eff}	1.73	1.65
Core-plasma radiation fraction, f_{rad}	0.48	0.49
^{4}He ash concentration (%)	8.58	10.0

[a]Density weighted.

3.5.3.1. Summary

The 1-D transport simulations using an empirically benchmarked tokamak plasma-transport model has confirmed that the ARIES-I plasma achieves ignition using the available current-drive power and achieves steady-state burn as long as the τ_E enhancement factor of 2.8 can be attained. Judging from the improvements in the empirical τ_E values achieved in tokamaks in the last 10 years, this level of confinement appears to be a reasonable extrapolation. The 1-D simulation results are in good agreement with 0-D predictions. Fueling remains an issue because pellets with reasonable sizes and speeds oblate in the outer parts of the plasma, and an anomalous inward pinch appears to be necessary to transport the fuel ions towards the plasma center.

The simulations also show that the Houlberg plasma-transport model not only predicts the plasma density and temperature profiles of certain TFTR and JET discharges accurately, but can also be extrapolated to power reactor conditions. It is important to note that while Houlberg's plasma-transport model predicts the density profiles used in the ARIES-I plasma analyses ($\alpha_n = 0.3$), there exist other transport models (*e.g.*, the theoretical transport model of Singer [25]) that predict even flatter density profiles for ARIES-I parameters. Future work in this area will involve a comparison between the models of Houlberg and Singer to decide which is more relevant to reactor-grade plasmas (comparison between Singer's model predictions and empirical results has been confined to ASDEX discharges).

3.6. SUMMARY AND CONCLUSIONS

The ARIES-I design is a conceptual commercial reactor based on modest extrapolation from the present tokamak physics data base. The ARIES-I design operates at a relatively high plasma aspect ratio ($A = 4.5$), a low plasma current ($I_p = 10.2$ MA), and a high on-axis magnetic field ($B_o = 11.3$ T). As a result, the poloidal beta is high and a high bootstrap-current fraction of 0.68 is predicted. Because of the low plasma current and high bootstrap-current fraction, only 3.3 MA of current should be driven by external means; therefore a steady-state reactor with relatively small current-drive power is possible. Systems-code analysis confirms that an optimum first-stability tokamak reactor operates with high aspect ratio, low current, and high bootstrap-current fraction. The key parameters of the ARIES-I reactor are listed in Table 3.1-I.

The ARIES-I MHD equilibrium, beta limit, vertical stability, and the plasma transport analyses have been described in this section. Generally only modest extrapolation

from the near-term physics data base is required. Some particular results of these studies indicate that:

- Diverted plasma with low elongation (1.8) can be created with relatively far-removed PF coils.
- Design iterations have led to a minimum stored-energy PF-coil set.
- A value for the Troyon beta coefficient of 3.2 is sufficient for first stability operation.
- Passive stabilization of short time-scale axisymmetric instabilities ($<$100 ms) is possible with the passive stabilizer elements located behind the blanket ($\sim 0.6a$ away from the plasma surface).
- Active stabilization of longer time-scale axisymmetric instabilities is possible with modest power demands (several MVAs).
- The first wall is weakly reflecting, which results in large synchrotron-radiation losses. This mode of operation reduces the divertor heat load.
- Energy-confinement enhancement factors of 2.5 to 3 times L-mode scaling (depending on the scaling model used) are needed to maintain the plasma power balance.

REFERENCES

[1] M. F. Reusch and G. H. Neilson, "Toroidally Symmetric Polynomial Multipole Solution of the Vector Laplace Equation," *J. Comput. Phys.* **64** (1986) 1416.

[2] C. E. Kessel, Jr. and M. A. Firestone, "Determination of Gross Plasma Equilibrium form Magnetic Multipoles," *Trans. Am. Nucl. Soc.* **52** (1986) 185.

[3] S. C. Jardin, N. Pomphrey, and J. DeLucia, "Dynamic Modeling of Transport and Positional Control of Tokamaks," *J. Comput. Phys.* **66** (1986) 481.

[4] D. J. Strickler *et al.*, "MHD Equilibrium Methods for ITER PF Coil Design and Systems Analysis," Oak Ridge National Laboratory report ORNL/FEDC-88/7 (1989); also D. J. Strickler, N. Pomphrey, and S. C. Jardin, "Equilibrium Shape Control in CIT PF Design," *Proc. IEEE 13th Symp. on Fusion Eng.,* Knoxville, TN (Oct. 1989), IEEE No. 89CH2820-9, IEEE, Piscataway, NJ (1990) p. 898.

[5] F. Troyon, R. Gruber, H. Sauernmann, S. Semenzato, and S. Succi, "MHD-Limits to Plasma Confinement," *Plasma Phys. and Controlled Fusion* **26** (1984) 209.

[6] T. Tsunematsu *et al.*, "Operational Limits and Disruptions in Tokamaks – Status and Application to ITER," Japan Atomic Energy Research Institute report JAERI-M-89-056 (1989).

[7] R. C. Grimm, J. M. Greene, and J. L. Johnson, "Computation of the Magnetohydrodynamic Spectrum in Axisymmetric Toroidal Confinement Systems," *Methods Comput. Phys.* **16** (1976) 253; also R. C. Grimm, R. L. Dewar, and J. Manickam, "Ideal MHD Stability Calculations in Axisymmetric Toroidal Confinement Systems," *J. Comput. Phys.* **49** (1983) 94.

[8] Y-K. M. Peng, J. C. Whitson, and A. H. Glasser, "Access to Second Ballooning Stability in Divertor Plasmas," *Bull. Am. Phys. Soc.* **34** (1989) 1971.

[9] M. W. Phillips, A. M. M. Todd, M. H. Hughes, *et al.*, "MHD Stability Properties of a High Current, High Beta Tokamak," *Nucl. Fusion* **28** (1988) 1499.

[10] J. A. Leuer, "Passive Vertical Stability in the Next Generation Tokamaks," *Fusion Tech.* **15** (1989) 489.

[11] D. J. Ward, S. C. Jardin, and C. Z. Cheng, "Stability of Axisymmetric Modes in Tokamak Plasmas with Active Feedback," *Bull. Am. Phys. Soc.* **34** (1989) 1974.

[12] C. Z. Cheng and M. S. Chance, "NOVA: A Nonvariational Code for Solving the MHD Stability of Axisymmetric Toroidal Plasmas," *J. Comput. Phys.* **71** (1987) 124.

[13] C. E. Singer *et al.*, "BALDUR: A One-Dimensional Plasma Transport Code," Princeton Plasma Physics Laboratory report PPPL-2073 (1986).

[14] K. J. Button and M. N. Afsar, "Millimeter Wave Dielectric Properties of Materials," *Proc. Int. Soc. for Optical Engineers,* San Diego, CA, *Millimeter Wave Technology II,* **423** (1983) 136.

[15] M. Bornatici, R. Cano, O. De Barbieri, and F. Engelmann, "Electron Cyclotron Emission and Absorption in Fusion Plasmas," *Nucl. Fusion* **23** (1983) 1153.

[16] S. Tamor, "SNECTR, a Code for Calculation of Transport of Cyclotron Radiation in Tokamaks," Science Applications Inc. report SAI-75-610LJ (1975); also S. Tamor, "SNECTR, a Cyclotron Radiation Transport Code: Current Status," Science Applications Inc. report SAI-76-773LJ (1976).

[17] S. Tamor, "A Simple Fast Routine for Computation of Energy Transport by Synchrotron Radiation in Tokamaks and Similar Geometries," Science Applications Inc. report SAI-023-81-189LJ (1981).

[18] S. Tamor, "Studies of Emission and Transport of Synchrotron Radiation in Tokamaks," Science Applications Inc. report SAI-023-81-110LJ (1981).

[19] B. A. Trubnikov, "Universal Coefficients for Synchrotron Emission from Plasma Configurations," *Reviews of Plasma Physics*, M. A. Leontovich, Ed., Consultants Bureau, New York (1979) Vol. 7, p. 345.

[20] W. Houlberg, Oak Ridge National Laboratory, private communication (June 1989).

[21] D. Stotler, Princeton Plasma Physics Laboratory, private communication (Jan. 1989).

[22] R. Goldston "CIT physics status update," Princeton Plasma Physics Laboratory, unpublished data (Dec. 1989).

[23] G. Bateman, Princeton Plasma Physics Laboratory, private communication (Dec. 1988).

[24] C. E. Singer, "Simulations of ARIES Reactors Using an Experimentally Calibrated Semi-Empirical $1\frac{1}{2}$-D Transport Model," University of Illinois, unpublished data (Aug. 1988).

[25] C. E. Singer *et al.*, "Multiple Mode Model of Tokamak Transport," Princeton Plasma Physics Laboratory report PPPL-2631 (1989).